SCIENTIFIC REPORTS

OPEN

Pronounced and reversible modulation of the piezoelectric coefficients by a low magnetic field in a magnetoelectric PZT-5%Fe$_3$O$_4$ system

G. Vertsioti[1,2], S. J. Zhang [3] & D. Stamopoulos[1,2]

Composite magnetoelectric compounds that combine ferroelectricity/piezoelectricity and ferromagnetism/magnetostriction are investigated intensively for room-temperature applications. Here, we studied bulk composites of a magnetostrictive constituent, ferromagnetic Fe$_3$O$_4$ nanoparticles, homogeneously embedded in a ferroelectric/piezoelectric matrix, Pb(Zr$_{0.52}$Ti$_{0.48}$) O$_3$ (PZT). Specifically, we focused on PZT-5%Fe$_3$O$_4$ samples which are strongly insulating and thus sustain a relatively high out-of-plane external electric field, $E_{ex,z}$. The in-plane strain-electric field curve (S($E_{ex,z}$)) was carefully recorded upon successive application and removal of an out-of-plane external magnetic field, $H_{ex,z}$. The obtained S($E_{ex,z}$) data exhibited two main features. First, the respective in-plane piezoelectric coefficients, d($E_{ex,z}$) = 200–250 pm/V, show a dramatic decrease, 50–60%, upon application of a relatively low $H_{ex,z}$ = 1 kOe. Second, the process is completely reversible since the initial value of d($E_{ex,z}$) is recovered upon removal of $H_{ex,z}$. Polarization data, P($E_{ex,z}$), evidenced that the Fe$_3$O$_4$ nanoparticles introduced *static structural disorder* that made PZT harder. Taken together, these results prove that the Fe$_3$O$_4$ nanoparticles, except for *static structural disorder*, introduce *reconfigurable magnetic disorder* that modifies the in-plane S($E_{ex,z}$) curve and the accompanying d($E_{ex,z}$) of PZT when an external magnetic field is applied at will. The room-temperature feasibility of these findings renders the PZT-x%Fe$_3$O$_4$ system a solid basis for the development of magnetic-field-controlled PE devices.

Electric field controlled phenomena have been extensively investigated, both experimentally and theoretically, during the past two decades in pristine compounds and composite systems that exhibit complex behavior in many of their physical properties (particle dynamics/interactions, optical, magnetic etc.) motivated by either extrinsic or intrinsic mechanism[1–5]. Regarding particle dynamics/interactions and the accompanying phase transitions, K. Kang studied in detail[1] systems of highly charged rod-like colloids. They showed that the particle interactions can be controlled by the application of an electric field, thus the phase diagram of relevant systems can be modulated at will. Referring to the optical properties, in a very recent work[2], S. Shian *et al.* described the correlation between electric field induced surface instabilities and light scattering for a compliant mat of carbon nanotubes on a smooth elastomer bilayer attached to an InSnO coated glass substrate. Interestingly, they observed that increasing the applied electric field, the optical transmittance decreases substantially, in a reversible way, a fact that can give rise to a wide spectrum of applications. Concerning the magnetic properties L. Bai *et al.* recently investigated[3] boron nitride nanotubes and proved that the application of an electric field causes reconstruction of the electronic bands, ultimately enabling us to transit between phases of different transport and magnetic properties. A relevant wide class of materials, either single phase or composites, are the so-called magnetoelectric (ME). In these materials the electric and magnetic polarization are coupled so that the application of an electric/

[1]Department of Solid State Physics, National and Kapodistrian University of Athens, Zografou Panepistimioupolis, Athens, Greece. [2]Institute of Nanoscience and Nanotechnology, National Center for Scientific Research 'Demokritos', Aghia Paraskevi, Athens, Greece. [3]Institute for Superconducting and Electronic Materials, Australian Institute of Innovative Materials, University of Wollongong, Wollongong, Australia. Correspondence and requests for materials should be addressed to D.S. (email: densta@phys.uoa.gr)
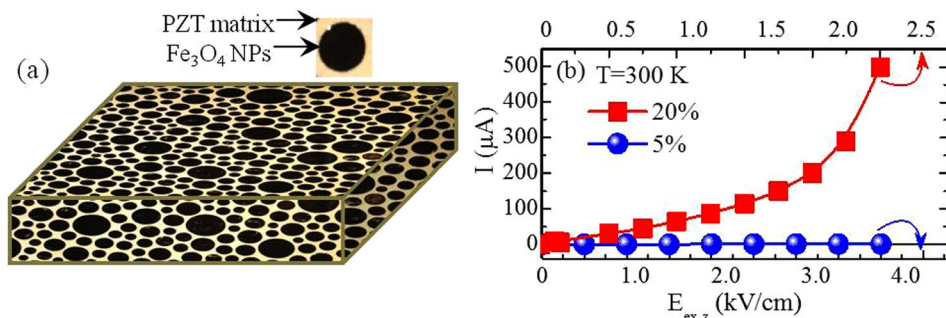
Figure 1. Schematic illustration and electric properties of the PZT-x%Fe$_3$O$_4$ samples. (**a**) Schematic illustration of the bulk PZT-x%Fe$_3$O$_4$ samples indicating that the Fe$_3$O$_4$ FM NPs are embedded in the PZT PE matrix. (**b**) Electric current leakage, I, under the application of an out-of-plane electric field, E$_{ex,z}$, for two PZT-xFe$_3$O$_4$ samples, with x = 5% and 20%. The bottom/top horizontal axis corresponds to the data referring to x = 5%/x = 20% sample.

magnetic field can control their magnetic/electric properties. Notably, the composite ME materials that are constructed of distinct ferroelectric (FE) and ferromagnetic (FM) building units can be designed at will and exhibit better performance when compared to the respective single phase ones. Specifically, ME materials that combine piezoelectric (PE) and FM constituents have recently earned great interest, since the coupling of their properties leads to large ME response upon the appearance of strain via an electric field, even at room temperature, a fact that is rarely met in single phase candidates[4,5]. For this reason, they find tremendous applications in functional devices such as information storage and magnetic field sensors[6–14]. Among this wide class of materials, the PE compound family Pb(Zr$_x$Ti$_{1−x}$)O$_3$ has been widely investigated, with special interest in the stoichiometry x ≈ 0.52, i.e. the Pb(Zr$_{0.52}$Ti$_{0.48}$)O$_3$ compound, that is the so-called morphotropic phase boundary[15–21]. Due to the coexistence of different crystallographic phases the specific Pb(Zr$_{0.52}$Ti$_{0.48}$)O$_3$ compound exhibits the maximum possible PE coefficients, d$_{ij}$. As a result, Pb(Zr$_x$Ti$_{1−x}$)O$_3$, in general, and Pb(Zr$_{0.52}$Ti$_{0.48}$)O$_3$, in particular, is widely employed as the PE constituent in ME composites, together with ferro/ferri-magnetic alloys and oxides, like CoFe$_2$O$_4$, Ni$_{0.93}$Co$_{0.02}$Mn$_{0.05}$Fe$_{1.95}$O$_4$, Ni$_{50}$Mn$_{35}$In$_{15}$, Co$_{1−x}$Zn$_x$Fe$_2$O$_4$ (x = 0.0–0.6), Ni$_{1−x}$Zn$_x$Fe$_2$O$_4$ (x = 0.0–0.5), CoFeO$_4$[22–27].

The above mentioned studies[22–27], as well as the majority of studies concerning ME composites[28–32], examine the electric-field control of the magnetic properties of the composites. The inverse, i.e. the control of FE or PE properties by an external magnetic field, H$_{ex}$, has been less investigated[33–36], focusing mostly on the electric polarization. Corresponding studies, performed by means of piezoresponse force microscopy, demonstrate the modulation of FE domains, upon application of an H$_{ex}$ on the order of 2–9 kOe. Among them, Evans et al.[35] and Xie et al.[36] based on Pb(Zr$_{1−x}$,Ti$_x$)O$_3$ as PE component, studied the changes in polarization[35] and piezoresponse[36] upon H$_{ex}$, for the cases of the ME composites PbZr$_{0.53}$Ti$_{0.47}$O$_3$-PbFe$_{0.5}$Ta$_{0.5}$O$_3$ (PZTFT) single crystals and PbZrTiO-TbDyFe (PZT-TDF) bilayer, respectively. These changes, were significant in magnitude, although partially reversible[35] or irreversible at all[36].

Apart from the polarization and piezoresponse, another basic PE parameter, the PE coefficients d$_{ij}$, have not been investigated upon application of an H$_{ex}$, until now. Here, we study the bulk composite system consisting of PE Pb(Zr$_{0.52}$Ti$_{0.48}$)O$_3$ (with composition at the so-called morphotropic phase boundary (MPB); called simply PZT for the rest of the paper) and FM Fe$_3$O$_4$ nanoparticles (NPs) that have noticeable magnetostrictive nature. Specifically, the FM NPs are embedded in the PE matrix in the desired weight percentage PZT-5%Fe$_3$O$_4$. We focus on the variation of the in-plane PE coefficients upon application of an E$_{ex,z}$ (ranging within ± 10 kV/cm) and a relatively low H$_{ex,z}$ (1 kOe), that are both applied out-of-plane at room temperature. By means of a method based on optical microscopy[37,38], we showed in a direct way that the application of such a low H$_{ex}$ = 1 kOe, causes a pronounced decrease of the in-plane PE coefficients on the order of 50–60%, that intriguingly is restored upon successive removal of H$_{ex}$. Polarization data showed that with the addition of the Fe$_3$O$_4$ NPs, PZT becomes harder when compared to its plain form. This is a proof that the FM NPs act as structural disorder that pins the FE domain walls efficiently, a fact that can be attributed to the similar size (50–100 nm) of the FM Fe$_3$O$_4$ NPs (see 'Sample preparation' in 'METHODS') and the FE domains of PZT (see[17,39–41]). These combined results prove that the FM Fe$_3$O$_4$ NPs serve not only as a simple *static structural disorder* but, most important, as a *reconfigurable magnetic disorder* that can be applied at will by means of an external magnetic field to control the PE properties of PZT. Based on the strong PE character of PZT and the noticeable magnetostrictive nature of Fe$_3$O$_4$, these findings can be ascribed to a strain transfer mechanism realized at the interface of the FM Fe$_3$O$_4$ NPs and the surrounding FE PZT matrix. Consequently, the quantitatively significant and qualitatively reversible modulation of the in-plane PE coefficients render PZT-5%Fe$_3$O$_4$ a candidate ME material for applications in functional devices with high ME performance.

Results and Discussion

A complete series of PZT-xFe$_3$O$_4$ samples (x = 0–50% w/w), that is Fe$_3$O$_4$ NPs homogeneously embedded in the PZT matrix as schematically shown in Fig. 1(a), was preliminary investigated to choose the appropriate insulating sample for the subsequent study. Obviously, a basic criterion is that the sample should remain strongly insulating for a reasonable range of electric field values. Figure 1(b), presents the leakage current as function of an electric
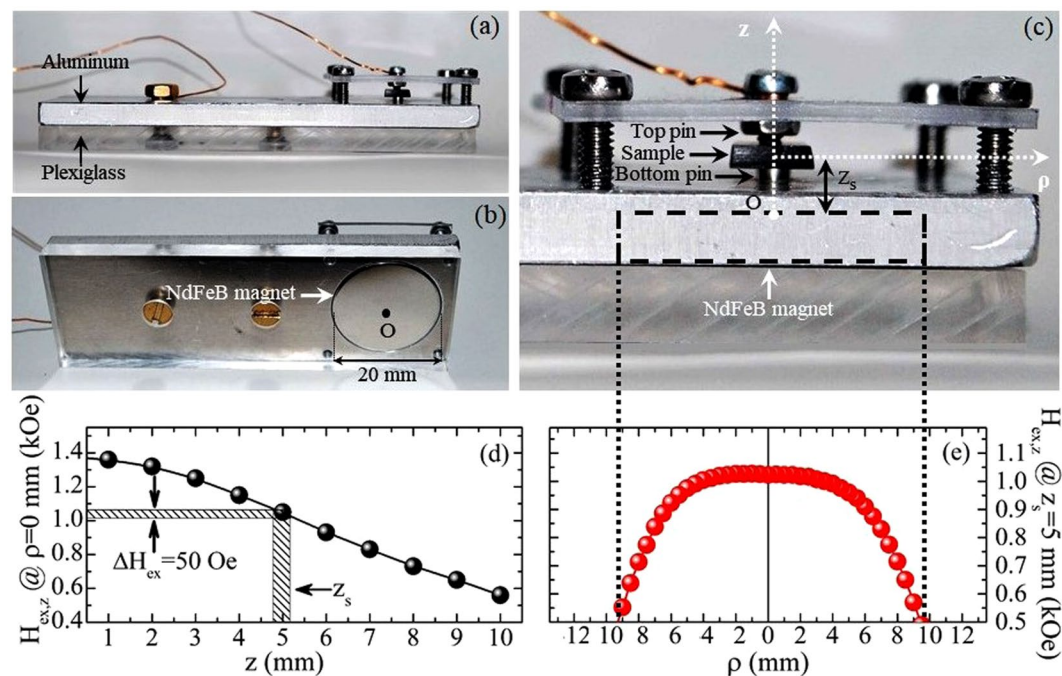
Figure 2. Home-made platform for the simultaneous application of the out-of-plane electric and magnetic fields, $E_{ex,z}$ and $H_{ex,z}$. (**a**) Side view and (**b**) perspective bottom view of the home-made platform constructed for the *local* observation of the sample, by means of an OM, under simultaneous application of an electric field, $E_{ex,z}$, produced by a DC-voltage supply and a constant magnetic field, $H_{ex,z}$, produced by a disc-shape NdFeB permanent magnet. $E_{ex,z}$ can be varied continuously within $-10\,$kV/cm to $+10\,$kV/cm during a set of measurements, while $H_{ex,z}$ is constant, 1 kOe, and exhibits azimuthal symmetry. (**c**) Detail of (**a**) in the sample area. The top and bottom pins hold the sample at its center so that the entire sample is left free to deform. The black dashed rectangle denotes the NdFeB magnet that is embedded in the aluminum platform, with its center, O, aligned with that of the sample (vertical dotted lines denote the boundary of the permanent magnet). The coordinate axes z and ρ are shown with white dotted lines. (**d**) Variation of $H_{ex,z}$ along the z coordinate ($\rho = 0\,$mm). (**e**) Variation of $H_{ex,z}$ along the ρ coordinate ($z_s = 5\,$mm).

field applied out-of-plane, $E_{ex,z}$, for two specific samples with x = 5% and x = 20%. We clearly see that the sample with x = 5% remains insulating, while the sample with x = 20% exhibits a noticeable leakage current for a comparatively much lower value of $E_{ex,z}$. Accordingly, all the experimental results presented below refer to PZT-5%Fe_3O_4.

The constitutive Strain-Electric field curve, $S(E_{ex,z})$, of samples PZT-5%Fe_3O_4 was estimated experimentally by using an OM-based technique already discussed in[37,38] for out-of-plane $E_{ex,z}$ up to 10 kV/cm. Here, we made another modification in the home-made aluminum platform hosting the sample, so that a constant, also out-of-plane magnetic field, $H_{ex,z}$, is applied at will, by a NdFeB permanent magnet, (disc-shaped with diameter 20 mm and thickness 3 mm). The magnet is placed just below the sample as shown in Fig. 2(a–c) and explained in detail at its caption. By means of this experimental setup, the in-plane strain curves, $S_{zx}(E_{ex,z})$ and $S_{zy}(E_{ex,z})$, can be recorded even under the presence of an $H_{ex,z}$ (see 'Section I' in Supplementary Information). We note that all materials used in this construction are non magnetic, else the magnetic field produced by the NdFeB permanent magnet would be non-homogeneous. Since our study aims to investigate the PE response upon the absence/presence of an external magnetic field, the homogeneity of $H_{ex,z}$ is crucial. In this context, accurate mapping of $H_{ex,z}$ was performed along the z coordinate, as shown in Fig. 2(d), and along the ρ coordinate, as shown in Fig. 2(e) (vertical dotted lines denote the boundary of the permanent magnet). The sample is placed at $z_s = 5\,$mm, with its center aligned with that of the magnet. Accordingly, the data of Fig. 2(d,e) prove that the external magnetic field of value $H_{ex,z}(z_s) = 1\,$kOe is fairly homogeneous over the entire volume of the PZT-5%Fe_3O_4 sample. This magnetic field brings the FM Fe_3O_4 NPs close to saturation (see magnetization data, below).

Detailed XRD data is shown in Fig. 3(a–c) on a comparative basis, with assignment of the main peaks, for non-sintered PZT-5%Fe_3O_4 (starting material: star. mat.), sintered PZT, sintered Fe_3O_4 NPs, and the sintered PZT-5%Fe_3O_4 composite (sintering conditions: T = 1000 °C, for t = 2 h in air). These results prove that (i) the magnetite, Fe_3O_4, is oxidized to hematite, α-Fe_2O_3, (partially, as evidenced by the magnetization data of Fig. 5, below), (ii) the MPB compositional PZT (Pb($Zr_{0.52}Ti_{48}$)O_3) undergoes a phase transition, probably promoted by the presence of Fe_3O_4, resulting in a coexistence of rhombohedral and tetragonal phases (evidenced by the peak broadening/splitting observed in the vicinity of 2θ = 22°, 31°, 45°, 50.5°, 56°, 65.5° and 74°, as highlighted by the grey-shaded areas)[20,42,43] and (iii) no byproducts/new compounds are present so that the former PZT-5%Fe_3O_4 system evolves to a PZT-5%(Fe_3O_4/α-Fe_2O_3) composite (for clarity, simply denoted PZT-5%Fe_3O_4 in the rest of the paper).
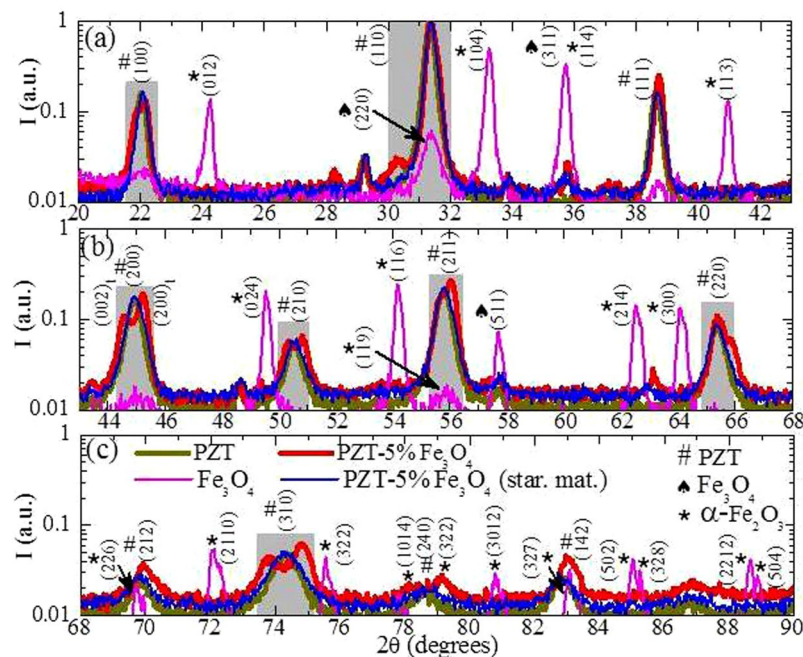
Figure 3. Characterization of crystallographic structure for non-sintered PZT-5%Fe$_3$O$_4$, sintered PZT, sintered Fe$_3$O$_4$ NPs, and sintered PZT-5%Fe$_3$O$_4$ samples. (**a–c**) XRD spectra presented in the 2θ range 20–90° for non-sintered PZT-5%Fe$_3$O$_4$ (starting material: star. mat.), sintered PZT, sintered Fe$_3$O$_4$ NPs, and the sintered PZT-5%Fe$_3$O$_4$ composite. The assignment of newly emerging peaks evidences the formation of hematite, α-Fe$_2$O$_3$, by the oxidation of the magnetite, Fe$_3$O$_4$, NPs. The assignment of broadened/splitted peaks (highlighted by the grey-shaded areas at 2θ = 22°, 31°, 45°, 50.5°, 56°, 65.5° and 74°) proves that PZT hosts both the rhombohedral and the tetragonal phases.
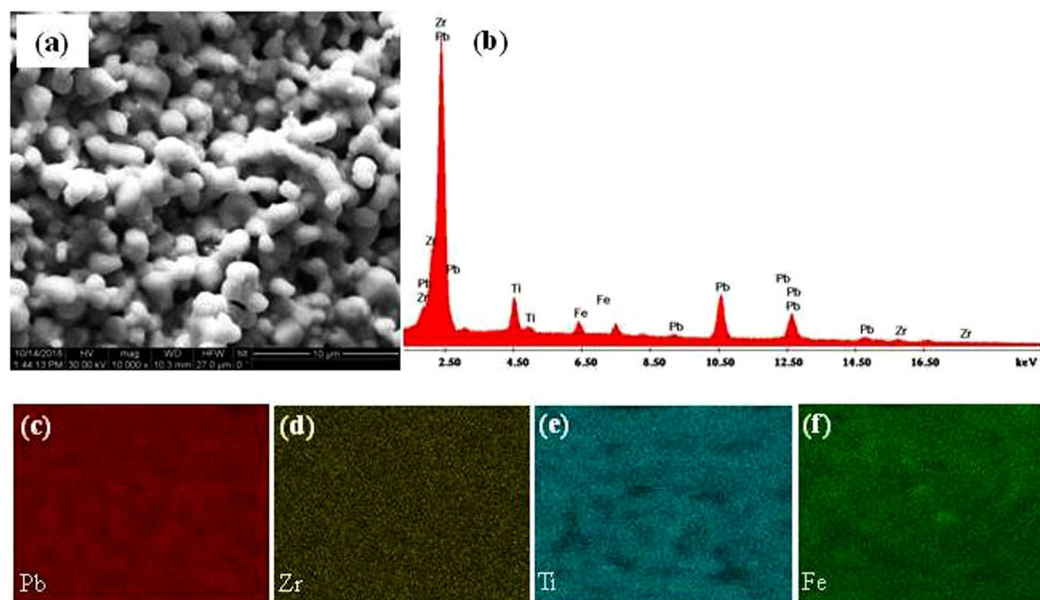

Figure 4. Characterization of microstructure and homogeneity of sintered PZT-5%Fe$_3$O$_4$. (**a–f**) SEM data for a sintered PZT-5%Fe$_3$O$_4$ composite in its as-prepared form (without polishing). (**a**) SEI topography image with magnification x10000. (**b**) BSE-based EDS spectrum for elemental analysis. (**c–f**) BSE-based EDS compositional mapping referring to (**c**) Pb, (**d**) Zr, (**e**) Ti, and (**f**) Fe.

Figure 4(a–f) present detailed SEM data referring to, topography (Fig. 4(a)), EDS spectrum for elemental analysis (Fig. 4(b)), and EDS elemental mapping (Fig. 4(c–f)) for a sintered PZT-5%Fe$_3$O$_4$ composite (sintering conditions: T = 1000 °C, for t = 2 h in air) in its as-prepared form (without polishing). These results prove that the
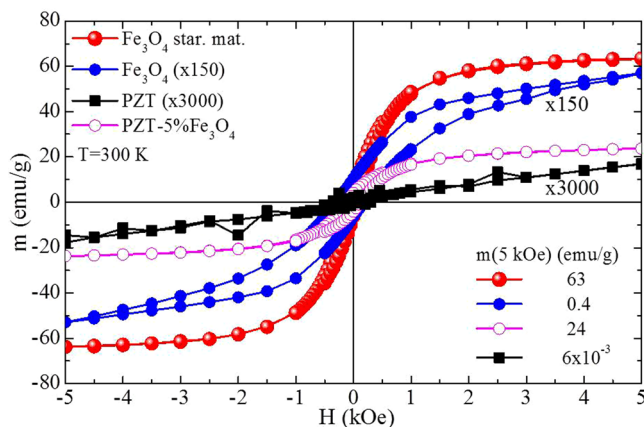
Figure 5. Magnetization data for non-sintered Fe_3O_4 NPs, sintered Fe_3O_4 NPs, sintered PZT, and sintered PZT-5%Fe_3O_4 samples. Magnetization curves, m(H), obtained in non-sintered Fe_3O_4 NPs (starting material: star. mat.), sintered Fe_3O_4 NPs, sintered PZT, and sintered PZT-5%Fe_3O_4 samples for an external magnetic field up to 5 kOe. The curve of sintered Fe_3O_4 NPs and sintered PZT is multiplied by a factor of 150 and 3000, respectively, for the sake of presentation. The magnetization value, m(5 kOe), obtained at the maximum applied magnetic field, 5 kOe, for each sample reads 63 emu/g for non-sintered Fe_3O_4 NPs, 0.4 emu/g for sintered Fe_3O_4 NPs, 6×10^{-3} emu/g for sintered PZT, and 24 emu/g for the sintered PZT-5%Fe_3O_4 composite.

sample is compact with the expected porosity, while all elements are uniformly distributed fairly well (we note that some inhomogeneity is expected since the composition of the sample is at the MPB). The respective data referring to a sintered PZT-5%Fe_3O_4 composite (sintering conditions: T = 1000 °C, for t = 2 h in air) after polishing are presented in Supplementary Information (see 'Section II').

The magnetization data of Fig. 5 accompany the XRD results and further support the conclusions discussed above. Specifically, Fig. 5 presents m(H) data for non-sintered Fe_3O_4 NPs (starting material: star. mat.), sintered Fe_3O_4 NPs, sintered PZT, and the sintered PZT-5%Fe_3O_4 composite (sintering conditions: T = 1000 °C, for t = 2 h in air). The deduced magnetization values for a magnetic field of 5 kOe are m = 63 emu/g, 0.4 emu/g, 6×10^{-3} emu/g, and 24 emu/g, respectively. We see that the non-sintered Fe_3O_4 NPs have high magnetization value, 63 emu/g, however lower than that of bulk magnetite due to their reduced size. When the Fe_3O_4 NPs are sintered in free form (not included in a PZT matrix) they completely oxidize to α-Fe_2O_3 as evidenced by the extremely lower magnetization value, 0.4 emu/g, obtained after sintering that is the magnetic fingerprint of hematite[44]. Referring to sintered PZT, it exhibits negligible magnetization, 6×10^{-3} emu/g, as expected. Accordingly, we can conclude that for the sintered PZT-5%Fe_3O_4 composite the deduced magnetization value, 24 emu/g, originates from Fe_3O_4 NPs that have not oxidized to α-Fe_2O_3 since they are protected by the PZT matrix. Using these magnetization values we can estimate that 38% of the NPs remain in the Fe_3O_4 form after sintering. In agreement to the XRD results the magnetization data show that the former PZT-5%Fe_3O_4 system evolves to a PZT-5%(Fe_3O_4/α-Fe_2O_3) composite (for clarity, simply denoted PZT-5%Fe_3O_4 in the rest of the paper).

Figure 6 shows detailed data of the in-plane PE coefficients obtained upon application and removal of a constant $H_{ex,z}$ for a square-shaped sample, (a.i)–(d.i), and for a disc-shaped sample, (a.ii)–(d.ii). The insets of the upper panels, (a.i) and (a.ii), show photos of the specific samples together with an arbitrarily chosen coordinate system that assists us to define the symmetry axes x (SA_x) and y (SA_y). As it should be, the investigated area was at the sample edge, in the specific case onto SA_y, as shown with a white dot for both samples (for details see 'Section III' of Supplementary Information and[37,38]). Concerning the experimental procedure, six consecutive $E_{ex,z}$ loops were recorded designated by a loop index; first, without the application of $H_{ex,z}$ (loop index: 1 and 2), next, under the presence of $H_{ex,z}$ = 1 kOe (loop index: 3 and 4) and finally, when removing $H_{ex,z}$ (loop index: 5 and 6). Figure 6(a.i,a.ii) present the mean absolute value of the in-plane PE coefficient in the y-direction, $<|d_{zy}|>$, for the complete sequence of measurements (the other in-plane PE coefficient in the x-direction, d_{zx}, is not shown since it is obviously zero[37,38]). Specifically, these panels present explicit data on $<|d_{zy}|>$ before applying (loop index: 1 and 2), upon application (loop index: 3 and 4) and after removal (loop index: 5 and 6) of a constant $H_{ex,z}$ = 1 kOe. For each loop the $<|d_{zy}|>$ is calculated from the slopes $|dS_{zy}/dE_{ex,z}|$ of the linear parts of the detailed $S_{zy}(E_{ex,z})$ data. Representative sets of the latter are shown in Fig. 6(b.i–d.i,b.ii–d.ii) for the square-shaped and disc-shaped sample, respectively, for loop index: 2 (without $H_{ex,z}$, (b.i) and (b.ii)), loop index: 4 (with $H_{ex,z}$, (c.i) and (c.ii)) and loop index: 6 (without $H_{ex,z}$, (d.i) and (d.ii)). The raw data of panels (c.i) and (d.i) are accessible in 'Section III' of Supplementary Information and the accompanying Supplementary Videos. Please note that, as expected[37,38], the respective $S_{zx}(E_{ex,z})$ loops are practically horizontal lines, since the investigated area was onto SA_y (see insets of Fig. 6(b.i–b.ii)). With the help of the raw data presented in Fig. 6(b.i–d.i)/(b.ii–d.ii), the main results of the present work become evident: first, the $S_{zy}(E_{ex,z})$ curves become narrower upon $H_{ex,z}$ application (Fig. 6(b.i)/(b.ii) vs Fig. 6(c.i)/(c.ii)), and second they recover their original form, almost completely, upon $H_{ex,z}$ removal (Fig. 6(b.i)/(b.ii) vs Fig. 6(d.i)/(d.ii)). Thus, this data evidences that the application of an external magnetic field, $H_{ex,z}$ = 1 kOe, causes drastic decrease to the respective in-plane PE coefficients on the order of 50–60% which is restored upon $H_{ex,z}$ removal, as summarized in the deduced $<|d_{zy}|>$ data that are presented in Fig. 6(a.i)/(a.ii).
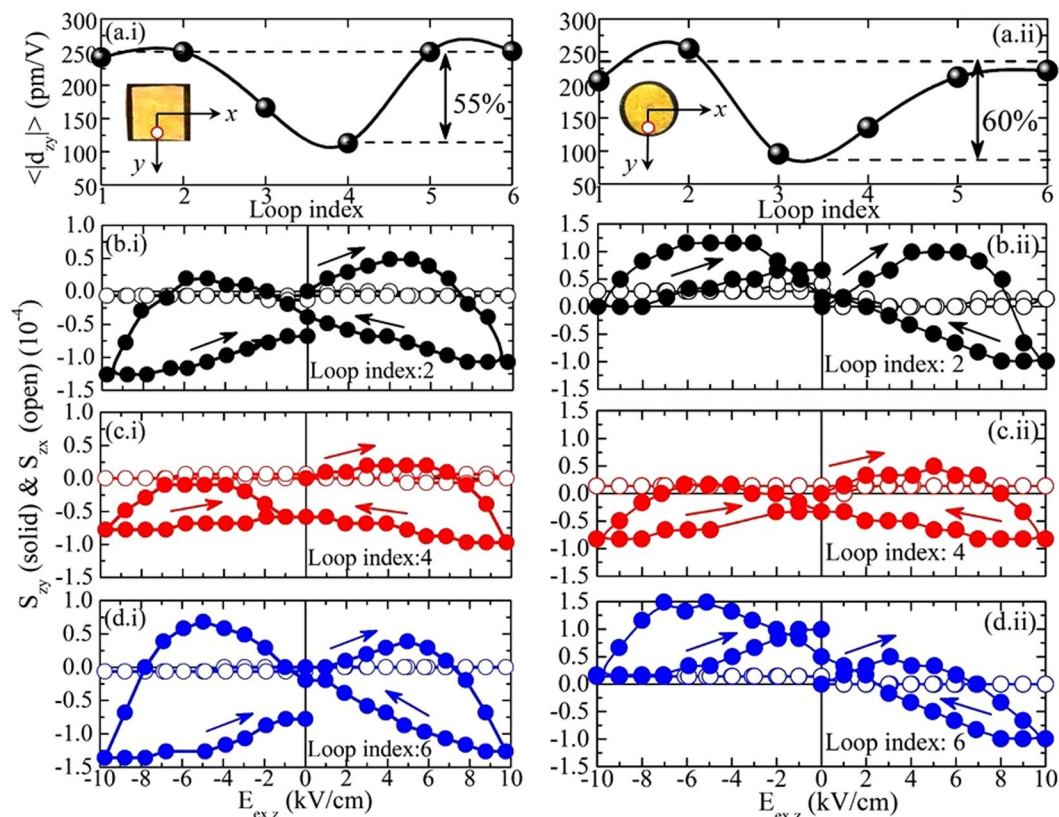
Figure 6. Piezoelectric data for PZT-5%Fe$_3$O$_4$ samples in the absence/presence of a constant out-of-plane magnetic field, H$_{ex,z}$. (**a.i–d.i**) & (**a.ii–d.ii**) Piezoelectric data for (**a.i–d.i**) square-shaped (length 7 mm, thickness 0.4 mm) and (**a.ii–d.ii**) disc-shaped (diameter 6 mm, thickness 0.4 mm), PZT-5%Fe$_3$O$_4$ samples. (**a.i,a.ii**) Mean value of PE coefficient originating for each case from the absolute values of the entire S$_{zy}$(E$_{ex,z}$) loop, $<|d_{zy}|>$, as function of H$_{ex,z}$ = 1 kOe; in the absence of H$_{ex,z}$ (Loop index: 1 & 2), under application of H$_{ex,z}$ (Loop index: 3 & 4) and after the removal of H$_{ex,z}$ (Loop index: 5 & 6). The inset photos show the respective samples together with the arbitrarily chosen x and y coordinate system. The investigated area is shown with a dot placed on SA$_y$ for both samples. (**b.i–d.i**)/(**b.ii–d.ii**) S$_{zy}$(E$_{ex,z}$) and S$_{zx}$(E$_{ex,z}$) loops, solid and open points respectively, for the square/disc-shaped sample upon application and removal of H$_{ex,z}$ = 1 kOe; (b.i)/(b.ii) in the absence of H$_{ex,z}$ (Loop index: 2), (**c.i**)/(**c.ii**) under application of H$_{ex,z}$ (Loop index 4) and (**d.i**)/(**d.ii**) after the removal of H$_{ex,z}$ (Loop index: 6). The arrows trace the sequence of E$_{ex,z}$ application. Please, notice that the vertical scale is the same in each group of three panels, (**b.i–d.i**) and (**b.ii–d.ii**). The raw data of panels (**c.i,d.i**) are accessible in 'Section III' of Supplementary Information and the accompanying Supplementary Videos.

To clarify the S$_{zy}$(E$_{ex,z}$) curves obtained with our local OM-based method we performed standard measurements of the polarization in both sintered PZT and PZT-5%Fe$_3$O$_4$ (sintering conditions: T = 1000 °C, for t = 2 h in air). Figure 7 shows raw P(E$_{ex,z}$) data, while its inset presents the derivative, dP/dE$_{ex,z}$, for the case of the PZT-5%Fe$_3$O$_4$ composite. From this data becomes apparent that the addition of the FM Fe$_3$O$_4$ NPs to PZT makes it harder; the P(E$_{ex,z}$) loop is noticeably broadened since the coercive field, E$_{ex,z}$^{coer}, increases from 6.7 kV/cm to 10.7 kV/cm. This fact can be ascribed to the efficient pinning of FE domain walls by the structural disorder introduced by the FM NPs; the similar size (50–100 nm) of the FM Fe$_3$O$_4$ NPs (see 'Sample preparation' in 'METHODS') and the FE domains of PZT (see[17,39–41]) can probably motivate and or promote this feature. On the other hand, the nucleation field, E$_{ex,z}$^{nuc}, is practically unaltered at approximately 4–5 kV/cm. Notably, the P(E$_{ex,z}$) data clearly show that the peaks observed in the S$_{zy}$(E$_{ex,z}$) curves of Fig. 6(b.i–d.i)/(b.ii–d.ii) correspond to the nucleation fields, E$_{ex,z}$$^{nuc,+}$ and E$_{ex,z}$$^{nuc,-}$, where FE domains appear and start to move/rotate, ultimately dictating complete reversal of the bulk polarization. Most important, the comparison of the S$_{zy}$(E$_{ex,z}$) results with the P(E$_{ex,z}$) ones clearly evidences that the FM Fe$_3$O$_4$/Fe$_2$O$_3$ NPs do not simply serve as *static structural disorder*; they introduce *reconfigurable magnetic disorder* that modifies the in-plane strain-electric field curves and the accompanying PE coefficients when an external magnetic field is applied at will.

Referring to the underlying mechanism motivating the observed ME coupling between the PZT matrix and the Fe$_3$O$_4$ NPs we recall that three mechanisms are generally considered: first charge modulation, second exchange interaction modulation and third strain transfer[45]. Since the first two mechanisms are active at a short range by a FE/FM interface, we suggest that the strain transfer mechanism is dominant in the case of the PE/FM PZT-5%Fe$_3$O$_4$ samples studied here (noticeably, the latter is active at length scales on the order of 100–200 nm[46,47]). Recently, A. Kumar *et al.*[48] employed the strain transfer mechanism to explain the results obtained in a relevant
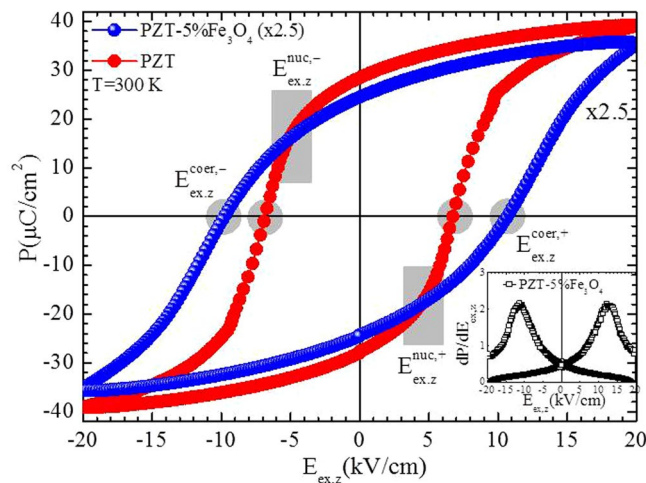
Figure 7. Polarization data for both PZT and PZT-5%Fe_3O_4 samples. Polarization curves, P($E_{ex,z}$), for both PZT and PZT-5%Fe_3O_4 samples for an external electric field along the z axis, $E_{ex,z}$, up to 20 kV/cm. The curve of the PZT-5%Fe_3O_4 sample is multiplied by a factor of 2.5 for the sake of presentation. The nucleation fields, $E_{ex,z}^{nuc,+}$ and $E_{ex,z}^{nuc,-}$ and coercive fields, $E_{ex,z}^{nuc,+}$ and $E_{ex,z}^{nuc,-}$ are marked with the gray-shaded areas. Inset presents the derivative, $dP/dE_{ex,z}$, for the case of the PZT-5%Fe_3O_4 composite.

multiferroic $BiFeO_3$-$BaTiO_3$ alloy system in which FM arises from a small fraction (~1 wt%) of $BaFe_{12}O_{19}$ that is formed during sintering. Interestingly, a very large increase (~34%) of the saturation polarization was observed under application of a magnetic field 10 kOe. The authors[48] attributed this finding to transfer of magnetostrictive strain from the FM $BaFe_{12}O_{19}$ grains to the adjacent ones of the FE phase. Specifically, since the magnetostriction coefficient, λ, of $BaFe_{12}O_{19}$ is negative (~ -1.5×10^{-5}) it was suggested that the contraction of the FM grains makes the FE ones to expand so that the pinning potential of the respective domain walls seemed to effectively reduce, ultimately enhancing their mobility[48]. In our case the same mechanism could be at play due to the strong PE character of PZT and the noticeable magnetostrictive nature of Fe_3O_4 and Fe_2O_3. Specifically, the magneto-striction coefficient, λ, of bulk magnetite ranges within 20×10^{-6} to 90×10^{-6} for single crystals and 30×10^{-6} to 50×10^{-6} for polycrystalline samples[49,50]. In addition, the magnetostriction coefficient of single crystals of bulk hematite is somehow lower, 10×10^{-6} at maximum[51]. For the case of NPs of Fe_3O_4 and Fe_2O_3 these values do not change except when considering ultra small ones with size 5 nm[52]. We see that the magnetostriction coefficient values of Fe_3O_4 and Fe_2O_3 are almost comparable to the PE coefficient ones of PZT (10^{-4}). Thus, we can assume that an effective interface strain transfer is realized between the Fe_3O_4 and Fe_2O_3 NPs (especially the Fe_3O_4 ones) and the surrounding PZT matrix. In this context, the magnetostrictive strain of Fe_3O_4 and Fe_2O_3 NPs (especially the Fe_3O_4 ones) can effectively alter the PE strain of the PZT matrix when an external magnetic field is applied. Indeed, the experimental fact that the PE coefficients are completely restored upon removal of the magnetic field (reversible procedure) hints that the underlying cause is a linear magnetostrictive effect of magnetoelastic nature.

Irrespectively of the underlying mechanism, here we report for the first time experimental data on the magnetic-field control of a ME parameter, specifically that of the PE coefficients d_{zi} (i = x,y), of three significant characteristics: first, it is impressive in magnitude, 60%, second, it is completely reversible, while third, and prob-ably most important, these characteristics are feasible at room temperature upon using a relatively low magnetic field, $H_{ex} = 1$ kOe. At this point, it is worth mentioning that recent studies[35,36] concerning composite ME systems report variations of similar magnitude in other relevant parameters such as the polarization and piezoresponse, but not in the PE coefficients reported here. In[35] D. M. Evans et al. report an average change of 60% in the polari-zation of PZTFT single crystals for a relatively high H_{ex} variation of 6 kOe, between the +3 kOe and −3 kOe states. Unfortunately, as already discussed by the authors[35], this noticeable percentage variation is partially reversible upon reversing once again the magnetic field back to +3 kOe, since the polarization attains a 40% higher value in comparison to that of the original state. In[36] S. H. Xie et al. observe a change of 40% in the piezoresponse of PZT-TDF bilayer upon application of +2 kOe. Notably, in contrast to the partially reversible behavior observed in[35], in[36] the authors report a further increase of the piezoresponse upon reversing the magnetic field to −2 kOe, a clear proof that in this case the overall process is entirely irreversible. The above comparative discussion with the data reported in[35,36] shout that our results could be important for applications at room temperature.

Conclusions

Here, we investigated the modulation of PE coefficients for a bulk PZT-5%Fe_3O_4 system, which is a strongly insulating hybrid of FM Fe_3O_4 NPs (noticeably magnetostrictive) homogeneously embedded in a FE PZT matrix (highly piezoelectric). By means of an OM-based method we recorded the in-plane strain loops for electric fields applied out-of-plane in the range -10 kV/cm $\leq E_{ex,z} \leq +10$ kV/cm, upon successive application and removal of an also out-of-plane external magnetic field of low value, $H_{ex,z} = 1$ kOe. The respective in-plane PE coefficients, 200–250 pm/V, display a dramatic decrease on the order of 50–60% upon $H_{ex,z}$ application, that is completely restored upon $H_{ex,z}$ removal. Polarization data performed in a wider range -20 kV/cm $\leq E_{ex,z} \leq +20$ kV/cm showed that

the addition of the FM Fe_3O_4 NPs makes the FE PZT harder obviously due to the pinning of FE domain walls by the newly introduced *static structural disorder*. The combined results clearly evidence that the FM Fe_3O_4 NPs do not simply serve as *static structural disorder*; they introduce *reconfigurable magnetic disorder* that modifies the in-plane strain-electric field curves and the accompanying PE coefficients when an external magnetic field is applied at will. Based on the strong PE character of PZT and the noticeable magnetostrictive nature of Fe_3O_4, these findings can be explained by a strain transfer mechanism realized at the interface of the FM Fe_3O_4 NPs and the surrounding FE PZT matrix. The high and entirely reversible modulation of the PE coefficients, under the application and removal of a low magnetic field, as well as the room temperature feasibility of the above advantages, render the PZT-x%Fe_3O_4 composite system or similar ones promising candidates for applications.

Methods

Sample Preparation.   The starting materials were $Pb(Zr_{0.52}Ti_{48})O_3$ powder, PZT5H type simply called PZT (NCE55, Noliac) and Fe_3O_4 (Sigma-Aldrich 98%, particle size: 50–100 nm). Fe_3O_4 powder in concentration x = 0–50% per weight, was grounded and mixed thoroughly with PZT powder into an agate mortar, in order to achieve homogeneous hybrid oxides. The mixed oxides were pressed into pellets at 35 MPa, with diameter 20 mm, placed on alumina crucibles and sintered at T_{sin} = 1000 °C, for t = 2 h, in air. The heating ($\approx$100 °C/h) and cooling ($\approx$50 °C/h) rates of the furnace (Carbolite Co. Ltd, UK) were kept constant for all the samples prepared. Here, we investigated samples of different shapes and dimensions. Specifically, the sintered PZT-x%Fe_3O_4 were cut at square-shaped sample with dimensions 7×7 mm^2 and disc shaped sample with diameter 6 mm. In order to apply external electric fields as high as $E_{ex,z}$ = 10 kV/cm, we reduced the thickness of the samples, t, from t = 1 mm down to t = 0.4 mm. To this end, the surfaces of the samples were polished using sandpaper, rinsed with ethanol and air dried. For $E_{ex,z}$ application, Au films (~100 nm) were sputtered on both surfaces of the samples (E5100, Quorum Technologies Ltd, Eats Sussex, UK), which also serve as reflective surfaces for observation with OM. During sputtering a macroscopic mask was employed to protect the lateral surfaces of the sample and avoid any short circuit while applying the external voltage. The samples were left unpoled.

Techniques.   Since the present study aims to attain information that could be of interest for practical applications it is exclusively focused at room temperature. As a consequence, all experimental techniques described below were employed at room temperature.

X-ray diffraction (XRD).   The compositional and structural characterization of $Pb(Z_{0.52}T_{0.48})O_3$, Fe_3O_4 and the hybrid composite $Pb(Zr_{0.52}Ti_{0.48})O_3$-5%$Fe_3O_4$ was obtained by means of XRD measurements performed with an X-ray diffractometer (D500, Siemens) that employs coupled θ–2θ scans with CuKα (wavelength λ = 1.5418 Å) as the radiation source.

Scanning Electron Microscopy (SEM).   SEM images were obtained by means of Inspect Microscope (FEI, Hillsboro, OR, USA) working with W (tungsten) filament. Regarding sample preparation, when necessary, PZT-5%Fe_3O_4 samples were sputtered with a thin layer (20–50 nm) of Au under medium vacuum (10^{-1} Torr) by means of a typical sputtering unit (E5100, Quorum Technologies Ltd, Eats Sussex, UK). Then the sample was placed onto conventional pin stubs. During SEM we employed typical values for the interfering parameters (i.e. acceleration voltage within 15–30 kV, working distance within 8–15 mm and spot size 3–8). Information on the topography for the evaluation of the microstructure was obtained with secondary electron imaging (SEI), while elemental analysis to obtain both energy-dispersive x-ray spectroscopy (EDS) information and compositional mapping images was recorded with backscattered electron imaging (BSE). Au-coated samples were used for SEI, while both Au-coated and non-coated samples were used for BSE to cross-check the results due to the overlapping of the M-spectral line of Au (2.123 keV) with the Lα-spectral line of Zr (2.044 keV) and the M-spectral line of Pb (2.342 keV).

Current-voltage (I–V) characteristics.   I–V characteristics were taken for the composite $Pb(Zr_{0.52}Ti_{0.48})O_3$-x%$Fe_3O_4$ samples, x = 0–50%, using a DC-voltage supply (model IP-32, Healthkit Co., USA) to apply the voltage across each sample, while *I* was monitored with the digital multimeter (MY-67, V&A). This information is important since we want to apply the maximum possible electric field to the sample without loss of its insulating properties.

Optical Microscopy for piezoelectric characterization.   The constitutive Strain-Electric field curve, $S(E_{ex,z})$, of the samples was estimated experimentally by using an OM-based technique introduced in[37]. An ORTHOLUX (Leitz, Wetzlar, Germany) OM was used, equipped with a linear xy translation stage on which a home-made aluminum platform was mounted. The magnification used was x100-x150 (objective lens x10). The calibration in the length scale of the OM images was accomplished by using the standard grating test TGZ3 (NT-MDT Co, Moscow, Russia). Using a DC-voltage supply (model IP-32, Healthkit Co., USA) we applied $E_{ex,z}$ up to 10 kV/cm along the sample thickness, i.e. out-of-plane, during the measurements. More details can be found in[38]. Here, we made another modification in the home-made aluminum platform hosting the sample, so that a constant magnetic field, $H_{ex,z}$, is applied at will, also out-of-plane (z axis), by a NdFeB permanent magnet, (disc-shaped with diameter 20 mm and thickness 3 mm). Mapping of $H_{ex,z}$ was performed with a Gaussmeter Model 410 (Lake Shore Cryotronics Inc, Ohio, USA), with its probe placed on a linear xyz stage with micrometer resolution.

Magnetization measurements. The constitutive Magnetization-Magnetic field curve, $M(H_{ex,z})$, of the samples was measured experimentally by using a SQUID magnetometer MPMS 5.5 Tesla (Quantum Design, San Diego, CA, USA).

Polarization measurements. The constitutive Polarization-Electric field curve, $P(E_{ex,z})$, of the samples was measured experimentally by using a TF Analyzer 2000 (aixACCT Systems GmbH, Aachen, Germany) ferroelectric analyzer connected with a high-voltage source Trek Model 610E (TREK INC, Lockport, NY, USA). The samples were immersed in silicone oil during the measurements to prevent arcing. The waveform and frequency of the applied electric field are triangle and 10 Hz, respectively.

References

1. Kang, K. Electric-field induced microdynamics of charged rods. *Front. Phys.* **2**, 73 (2014).
2. Shian, S., Kjeer, P. & Clarke, D. R. Electric-field induced surface instabilities of soft dielectrics and their effects on optical transmittance and scattering. *J. Appl. Phys.* **123**, 113105 (2018).
3. Bai, L., Gu, G., Xiang, G. & Zhang, X. Electric-Field-Induced Spontaneous Magnetization and Phase Transitions in Zigzag Boron Nitride Nanotubes. *Sci. Rep.* **5**, 12416 (2015).
4. Nan, C. W., Bichurin, M. I., Dong, S., Viehland, D. & Srinivasan, G. Multiferroic magnetoelectric composites: Historical perspective, status and future directions. *J. Appl. Phys.* **103**, 031101 (2008).
5. Ruy, J., Priya, S., Uchino, K. & Kim, H. E. Magnetoelectric effect in composites of magnetostrictive and piezoelectric materials. *J. Electroceram.* **8**, 107–119 (2002).
6. Xiao, Z. *et al.* Bi-directional coupling in strain-mediated multiferroic heterostructures with magnetic domains and domain wall motion. *Sci. Rep.* **8**, 5207 (2018).
7. Eerenstein, W., Mathur, N. D. & Scott, J. F. Multiferroic and magnetoelectric materials. *Nature* **442**, 759–765 (2006).
8. Ma, J., Hu, J., Li, Z. & Nan, C. W. Recent progress in multiferroic magnetoelectric composites: from bulk to thin films. *Adv. Mater.* **23**, 1062–1087 (2011).
9. Ortega, N., Kumar, A., Scott, J. F. & Katiyar, R. S. Multifunctional magnetoelectric materials for device applications. *J. Phys.: Condens. Matter.* **27**, 504002 (2015).
10. Scott, J. F. M. M. *Nat. Mater.* **6**, 256–257 (2007).
11. Fiebig, M. Revival of magnetoelectric effect. *J. Phys. D: Appl. Phys.* **38**, R123–R152 (2005).
12. Hu, J. M., Nan, T., Sun, N. X. & Chen, L. Q. Multiferroic magnetoelectric nanostructures for novel device applications. *MRS Bull.* **40**, 728–735 (2015).
13. Wang, Y., Li, J. & Viehland, D. Magnetoelectrics for magnetic sensor applications: status, challenges and perspectives. *Mater. Today1* **7**, 269–275 (2014).
14. Ahmed, R. & Victora, R. H. A fully electric driven scalable magnetoelectric switching element. *Appl. Phys. Lett.* **112**, 182401 (2018).
15. Noheda, B. *et al.* A monoclinic ferroelectric phase in the $Pb(Zr_{1-x}Ti_xO_3)$ solid solution. *Appl. Phys. Lett.* **74**, 14 (1999).
16. Guo, R. *et al.* Origin of high piezoelectric response in $PbZr_{1-x}Ti_xO_3$. *Phys. Rev. Lett.* **84**, 5423–5426 (2000).
17. Randall, C. A., Kim, N., Kucera, J.-P., Cao, W. & Shrout, T. R. Intrinsic and extrinsic size effects in fine-grained morphotropic-phase-boundary lead zirconate titanate ceramics. *J. Am. Ceram. Soc.* **81**, 677–688 (1998).
18. Zhang, N. *et al.* The missing boundary in the phase diagram of $PbZr_{1-x}Ti_xO_3$. *Nat. Commun.* **5**, 5231 (2014).
19. Cordero, F. Elastic properties and enhanced piezoelectric response at morphotropic phase boundaries. *Materials* **8**, 8195–8245 (2015).
20. Singh, A. P., Mishra, S. K., Lal, R. & Pandey, D. Coexistence of tetragonal and rhombohedral phases at the morphotropic phase boundary in pzt powders i. x-ray diffraction studies. *Ferroelectrics* **163**, 103–113 (1995).
21. Burianova, L., Sulc, M. & Prokopova, M. Determination of the piezoelectric coefficients d_{ij} of PZT ceramics and composites by laser interferometry. *J. Eur. Ceram. Soc.* **21**, 1387–1390 (2001).
22. Dipti, Juneja, J. K., Singh, S., Raina, K. K. & Prakash, C. Enhancement in magnetoelectric coupling in PZT based composites. *Ceram. Int.* **41**, 6108–6112 (2015).
23. Park, J. H., Kim, M. G., Ahn, S. J., Ryu, S. & Jang, H. M. Interfacial strain-mediated magnetoelectric coupling as reflected in extended X-ray absorption spectra of $CoFe_2O_4$-dispersed $Pb(Zr,Ti)O_3$ matrix composites. *J. Magn. Magn. Mater.* **321**, 1971–1974 (2009).
24. Narendra Babu, S., Suryanarayana, S. V. & Bhimasankaram, T. Magnetic and magnetoelectric characterization of $Ni_{0.93}Co_{0.02}Mn_{0.05}Fe_{1.95}O_4$ and PZT composites. *J. Alloys Compd.* **473**, 418–422 (2009).
25. Signh, K. & Kaur, D. Room-temperature giant magneto-mechanical-electric cross-coupling in Si-integrated $Pb(Zr_{0.52}Ti_{0.48})O_3$/ $Ni_{50}Mn_{35}In_{15}$ multiferroic heterostructures. *J. Phys. D: Appl. Phys.* **50**, 14 (2017).
26. Srinivasan, G., Rasmussen, E. T. & Hayes, R. Magnetoelectric effects in ferrite-lead zirconate titanate layered composites: The influence of zinc substitution in ferrites. *Phys. Rev. B* **67**, 014418 (2003).
27. Boni, A. G. *et al.* Steplike switching in symmetric $PbZr_{0.2}Ti_{0.8}O_3$/$CoFeO_4$/$PbZr_{0.2}Ti_{0.8}O_3$ heterostructures for multistate ferroelectric memory. *Phys. Rev. Appl.* **8**, 034035 (2017).
28. Geprags, S., Bandlmaier, A., Opel, M., Gross, R. & Goennenwein, S. T. B. Electric-field controlled manipulation of the magnetization in $Ni/BaTiO_3$ hybrid structures. *Appl. Phys. Lett.* **96**, 142509 (2010).
29. Brivio, S., Petti, D., Bertacco, R. & Cezar, J. C. Electric field control of magnetic anisotropies and magnetic coercivity in $Fe/BaTiO_3$ (001) heterostructures. *Appl. Phys. Lett.* **98**, 092505 (2011).
30. Lahtinen, T. H. E., Franke, K. J. A. & van Dijken, S. Electric-field control of magnetic domain wall motion and local magnetization reversal. *Sci. Rep.* **2**, 258 (2012).
31. Xiong, Y. Q. *et al.* Electric field modification of magnetism in $Au/La_{2/3}Ba_{1/3}MnO_3/Pt$ device. *Sci. Rep.* **5**, 12766 (2015).
32. Hu, Z. *et al.* Voltage control of magnetism in FeGaB/PIN-PMN-PT multiferroic heterostructures for high-power and high-temperature applications. *Appl. Phys. Lett.* **106**, 022901 (2015).
33. Li, L. *et al.* Direct observation of magnetic field induced ferroelectric domain evolution in self-assembled quasi (0–3) $BiFeO_3$—$CoFe_2O_4$ thin films. *ACS Appl. Mater. Interfaces* **8**, 442–448 (2016).
34. Miao, H., Zhou, X., Dong, S., Luo, H. & Li, F. Magnetic-field-induced ferroelectric polarization reversal in magnetoelectric composites revealed by piezoresponse force microscopy. *Nanoscale* **6**, 8515–8520 (2014).
35. Evans, D. M. *et al.* Magnetic switching of ferroelectric domains at room temperature in multiferroic PZTFT. *Nat. Commun.* **4**, 1534 (2013).
36. Xie, S. H. *et al.* Local two-way magnetoelectric couplings in multiferroic composites via scanning probe microscopy. *J. Appl. Phys.* **108**, 054108 (2010).
37. Stamopoulos, D. & Zhang, S. J. A method based on optical and atomic force microscopes for instant imaging of non-homogeneous electromechanical processes and direct estimation of d_{ij} coefficients in piezoelectric materials at local level. *J. Alloys Compd.* **612**, 34–41 (2014).
38. Zeibekis, M., Vertsioti, G. & Stamopoulos, D. On the optimum processing conditions of $Pb(Zr_xTi_{1-x})O_3$: revealing the mechanisms to increase the piezoelectric coefficients up to 1100 pmV^{-1}. *J. Phys. D: Appl. Phys.* **49**, 105304 (2016).

39. Cao, W. & Randall, C. A. Grain size and domain size relations in bulk ceramic ferroelectric materials. *J. Phys. Chem. Solids* **57**, 1499–1505 (1996).
40. Gruverman, A. *et al.* Nanoscale imaging of domain dynamics and retention in ferroelectric thin films. *Appl. Phys. Lett.* **71**, 24 (1997).
41. Mishra, S. K. & Pandey, D. Effect of particle size on the ferroelectric behaviour of tetragonal and rhombohedral Pb(Zr$_x$Ti$_{1-x}$)O$_3$ ceramics and powders. *J. Phys.: Condens. Matter* **7**, 9287–9303 (1995).
42. Helbig, U. Size effect in low grain size neodymium doped PZT ceramics. *J. Eur. Ceram. Soc.* **27**, 2567–2576 (2007).
43. Mirzaei, A., Bonyani, M. & Torkian, S. Effect of Nb doping on sintering and dielectric properties of PZTceramics, Process. *Appl. Ceram.* **10**, 175–182 (2016).
44. Cornell, R. M. & Schwertmann, U. *The Iron oxides: Structure, Properties, Reactions, Occurences and Uses (WILEY-VCH Verlag GmbH & Co, 2003)*.
45. van Dijken, S. *Handbook of* Spintronics Vol. *1 (eds Xu, Y. et al.) Ch. 10, 365–398 (Springer Netherlands, 2015)*.
46. Kim, J. Y., Yao, L. & van Dijken, S. Coherent piezoelectric strain transfer to thick epitaxial ferromagnetic films with large lattice mismatch. *J. Phys.: Condens. Matter* **25**, 082205 (2013).
47. Biegalski, M. D., Dorr, K., Kim, D. H. & Christen, H. M. Applying uniform reversible strain to epitaxial oxide films. *Appl. Phys. Lett.* **96**, 151905 (2010).
48. Kumar, A., Narayan, B., Pachat, R. & Ranjan, R. Magnetic enhancement of ferroelectric polarization in a self-grown ferroelectric-ferromagnetic composite. *Phys. Rev. B* **97**, 064103 (2018).
49. Bickford, L. R., Pappis, J. & Stull, J. L. Magnetostriction and Permeability of Magnetite and Cobalt-Substituted Magnetite. *Phys. Rev.* **99**, 1210 (1955).
50. Moskowitz, B. M. High-Temperature Magnetostriction of Magnetite and Titanomagnetites. *J. Geophys. Res.* **98**, 359 (1993).
51. Urquhart, H. M. A. & Goldman, J. E. Magnetostrictive Effects in an Antiferromagnetic Hematite Crystal. *Phys. Rev.* **101**, 1443 (1956).
52. Balaji, G., Aravinda Narayanan, R., Weber, A., Mohammad, F. & Kumar, C. S. S. R. Giant magnetostriction in magnetite nanoparticles. *Mater. Sci. Eng. B* **177**, 14 (2012).

Acknowledgements

Author Contributions

D.S. conceived and coordinated the study. G.V. prepared all samples and performed most of the measurements. S.Z. and D.S. performed part of the measurements. G.V., S.Z. and D.S. analyzed the experimental data. G.V. and D.S. drafted the manuscript. G.V., S.Z. and D.S. revised the manuscript.

Additional Information

Supplementary information accompanies this paper at https://doi.org/10.1038/s41598-019-38675-8.

Competing Interests: The authors declare no competing interests.

Publisher's note: Springer Nature remains neutral with regard to jurisdictional claims in published maps and institutional affiliations.